REVIEW ARTICLE

Helium ion microscopy

Gregor Hlawacek,[a] Vasilisa Veligura, Raoul van Gastel, and Bene Poelsema
Physics of Interfaces and Nanomaterials, MESA+ Research Institute, University of Twente, PO Box 217, 7500AE Enschede, The Netherlands

(Received 7 November 2013; accepted 14 January 2014; published 6 February 2014)

Helium ion microcopy based on gas field ion sources represents a new ultrahigh resolution microscopy and nanofabrication technique. It is an enabling technology that not only provides imagery of conducting as well as uncoated insulating nanostructures but also allows to create these features. The latter can be achieved using resists or material removal due to sputtering. The close to free-form sculpting of structures over several length scales has been made possible by the extension of the method to other gases such as neon. A brief introduction of the underlying physics as well as a broad review of the applicability of the method is presented in this review. © *2014 American Vacuum Society*. [http://dx.doi.org/10.1116/1.4863676]

I. INTRODUCTION

High resolution imaging, in particular, in biology and materials science, is mostly done using scanning electron microscopy (SEM). The ease of use and the widespread availability has made this the number one method for imaging in the aforementioned fields. Structuring and manipulation of nanosized features is traditionally the domain of focused ion beams (FIBs). Here, mainly liquid metal ion sources (LMIS) using gallium are used. However, other techniques such as various types of gas field ion sources (GFIS),[1] alloy LMIS,[2] magneto optical trap sources,[3] and multicusp plasma sources[4] are runners-up. Good reviews discussing these two techniques can be found in Refs. 5 and 6 for SEM and FIB, respectively.

Helium ion microscopy presents a technique that unites many of the advantages of SEM and FIB in a single tool. More importantly, it also overcomes some of the deficiencies of SEM and FIB. In particular, the possibility to image biological and in general insulating samples without coating at highest resolution is important for many scientific questions currently discussed in materials science and biology. Another important charged particle beam technique—namely, transmission electron microscopy (TEM)—depends on very thin samples free of defects from the preparation. The unique nanosized beam of the helium ion microscopy (HIM) makes it possible to not only mill and pattern smallest features but also do this with minimal damage to the crystal lattice.

In the following, we will give an outline of the working principle and signal generation in helium ion microscopy, followed by two sections highlighting specific imaging applications and examples of materials modification.

A. Working principle

The initial idea of a scanning ion microscope has been put forward by Knoll and Ruska already in 1932.[7] The working principle of a helium ion microscope can be divided into three different stages:

(1) Helium ionization and acceleration
(2) Beam formation and control
(3) Sample interaction.

In this introduction, we will only briefly touch points 1 and 2. Instead, we will focus on the physics that is important to understand the application of the technique to imaging and nanofabrication.

The first is made possible by using a newly developed GFIS. GFIS have been investigated for a long time[1,8–10] for their use in microscopes.[11–14] The idea is based on the initial design of a field ion microscope by Müller.[15,16] However, only recently, a stable ion source with a high brightness and small virtual source size has been realized by Ward, Notte, and Economou for use in a microscope.[17] It is based on an emitter whose apex has been shaped into a three sided pyramid (see Fig. 1). Work is done currently to understand and optimize the supertip formation process in order to maximize the achievable current.[18–23] Using scanning field ion microscopy (SFIM), the apex of the tip can be monitored and shaped using high fields that can ultimately remove weakly bound atoms from the apex. In this way, the configuration of the tip apex can be controlled at the atomic level. Although monomers are possible, trimers are more stable. Figure 1(b) shows a SFIM image of the tip. The trimer in the center and the edge of the first shelf below the trimer are visible. The combination of a pyramidally shaped tip and the carefully shaped apex concentrates the electric field, so that subsequent helium ionization predominantly happens at the top most atoms of the pyramid. Using apertures in the beam path allows to select current originating from ionization events on a single apex atom. Typical source parameters are listed in Table I.

[a]Author to whom correspondence should be addressed; electronic mail: g.hlawacek@utwente.nl

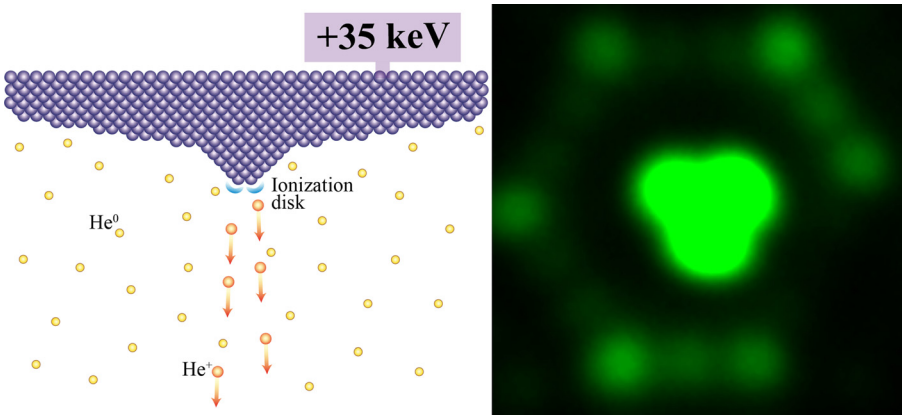

FIG. 1. (Color online) (a) Sketch of a GFIS. Ionization happens dominantly at the most protruding corner and edge atoms. (b) Actual SFIM image of a GFIS. The center trimer and the edges and corners of the next crystal plane are visible.

The second point is technologically demanding and requires a high degree of knowledge on the design and implementation of the involved electrostatic lenses, quadrupoles, octopoles, etc. For more details, the reader is referred to numerous monographs available on charged particle optics.[24,25] The critical source parameters important for the ion optical performance of the column are given in Table I. The energy spread of 1 eV is an upper bound. Earlier measurements indicate that the values could in fact be lower by a factor of two to four.[26] One of the important consequences of the parameters listed in Table I is the image side beam convergence angle α_i. Typical values for α_i are well below 1 mrad. This small beam divergence results in a large depth of field

$$d_f = \frac{\delta}{\alpha_i}. \tag{1}$$

Here, δ denotes the minimum feature that can be resolved in the image. Assuming identical resolutions the HIM will have a superior depth of field as compared to low-voltage SEM with typical α_i values of 8 mrad.[27]

Once the focused ion beam strikes the sample, the interaction of the accelerated particles with the substrate atoms and electrons will give rise to a large number of different signals. We will cover the available signals in the following section. Before we do so, we will briefly discuss the processes that occur during ion/sample interaction and that are important for the achievable resolution in charged particle beam imaging. Besides the small beam diameter, the shape and size of the actual interaction volume between the impinging particle and the sample plays an important role to reach ultimate resolution. Figure 2 compares Monte Carlo simulation results for different charged particle beams. From the figure, it is evident that the interaction volume relevant for secondary electron (SE) generation of the focused He beam is smaller than for the other two.[28] For the case of a Ga beam, the large cross section of Ga with—in this case—Si leads to substantial scattering in the near surface region relevant for the SE signal generation. For a low energy electron beam—needed to simultaneously optimize resolution and surface sensitivity in SEM—electron–electron scattering in the sample widens the beam dramatically in the first few nanometers deteriorating the achievable resolution. Scattering also occurs in HIM. In the case of a 30 keV He beam, scattering occurs with the nuclei of the sample atoms. However, due to the low mass of helium, scattering is not very efficient in the first few nanometers of sample material. This results in minimal beam divergence inside the sample. Consequently, the collected SE originate from a cylinder with a minimal volume. The somewhat lower energy of the SE in HIM[29] and the lower characteristic escape depth for SE in HIM for light elements[30] enhances this difference between SEM and HIM even further.

TABLE I. Typical helium ion source parameters (Ref. 141).

Virtual source size	$\leq$0.25 nm	Estimated
Angular intensity	0.5–1 μA sr^{-1}	Measured
Brightness	$\approx 1 \times 10^9$ A cm^{-2} sr^{-1}	Calculated
Energy spread	1 eV (0.25–0.5 eV)[26]	Measured

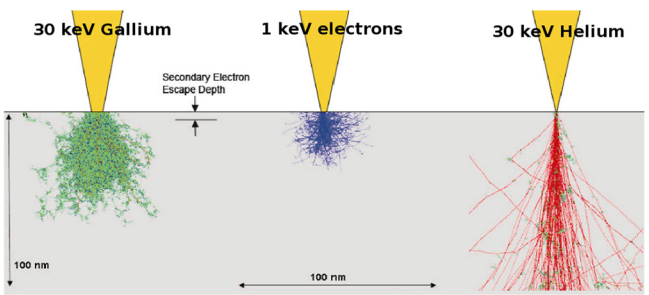

FIG. 2. (Color online) Comparison of the interaction volume of different charged particles beams used for imaging. The substrate material is silicon in all cases. The typical escape depth of secondary electrons is indicated. From left to right, first the interaction volume of a 30 keV gallium beam is shown. Such a beam is typically used in FIB applications. In the center, a low energy electron beam of 1 keV is presented. The energy is specifically chosen to maximize both surface sensitivity and resolution simultaneously. Finally, a 30 keV He beam—typically used in HIM to obtain maximum resolution—is presented. Ion trajectories have been obtained from SRIM (Ref. 90). The electron trajectories have been calculated by CASINO (Ref. 140). Reprinted with permission from AIP Conf. Proc. **931**, 489 (2007). Copyright 2007, AIP Publishing LLC.

B. Signals

Next, we will discuss available particles and corresponding signals. We will in particular highlight their benefits and drawbacks when used for imaging and what kind of physical quantities can be accessed using them. The sequence in which they are discussed is determined by their abundance in the tool. This also corresponds to the ease of use and how widespread the technique is available in the current instrument base. An initial overview of some of the different contrast mechanisms is given by Bell.[31,32]

1. Secondary electrons

Secondary electron (SE) emission generated by ions can be split into two parts. In the logical order, we will first discuss SE generation followed by the transport of electrons through the material. The latter is important as the generated electrons still need to reach and subsequently leave the surface into the vacuum so they can be detected. As has been proposed by Bethe,[33] the rate of secondary electron generation δ_{SE} (electrons per incoming ion) is proportional to the stopping power of the incident particle $\mathrm{d}E/\mathrm{d}s$ in eV/Å

$$\delta_{\mathrm{SE}} = -\frac{1}{\epsilon}\frac{\mathrm{d}E}{\mathrm{d}s}. \tag{2}$$

Here, ϵ denotes a scaling constant. It is assumed that at least in the relevant near surface region, atomic collisions do not play an important role and $\mathrm{d}E/\mathrm{d}s$ depends only on the electronic stopping power.

The generated SE1 are mostly excited by the incoming ions via kinetic emission (KE).[34] Two types of secondary electrons of type 2 (SE2) exist in ion beam imaging. Type 2 electrons can be generated either by recoiling target atoms or from other SEs of type 1. The second type of SE2 generation (SE generated by SE) does not play an important role in HIM. This becomes clear when looking at the maximum energy of the SE, which is taken to be equal to the energy loss of the impinging He for a head-on collision[34,35]

$$\Delta E = 2m_e(v + (v_F/2))^2. \tag{3}$$

Here, m_e is the electron mass, v the ion velocity, and v_F denotes the Fermi-velocity. The cross section for such a collision is highest if the ion velocity—$v \approx 1.3 \times 10^6$ m/s for a primary energy of 35 keV—matches the Fermi-velocity of the electrons in the material. For gold and 35 keV He, this yields a maximum SE energy of 45 eV. However, this energy is approximately equal to—or even below—the effective energy needed for SE generation by electrons in many materials.[36] Thus, the size of the electron–electron collision cascade is restricted.

However, kinetic excitation of electrons is also possible by recoil atoms, provided they are fast enough so that their speed still matches the Fermi-velocity of the target material. Electrons produced by recoiling target atoms are usually called SE2. Ramachandra *et al.*[30] calculated the ratio between SE2 and SE1 as function of energy and material. The conclusion that can be drawn from their calculation is that for higher primary energies a smaller SE2/SE1 ratio can be achieved for most materials and consequently a higher resolution is possible.

The other process for electron emission is potential emission (PE) via Auger neutralization. However, only for very low energies below 5 keV, PE becomes dominant[30,37] over KE.

Once secondary electrons have been generated they still need to escape from the solid. This process can be described as a diffusion process. The characteristic length scale of this diffusion process—the effective diffusion length of secondary electrons λ_d—is of the order of 1 nm for nearly all materials.[30] This leads to the fact that only the first few nanometers of the material add to the emitted SEs. Measurements of the effective SE yield in HIM show variations between 1 for carbon and values as high as 8 for platinum.[28]

The number and energy distribution of these ion induced secondary electrons differs from what is found in a SEM. A sharper maximum at lower energies is usually found[38,39] in HIM. In Fig. 3(a), a comparison of calculated SE yields in SEM, Ga-FIB, and HIM is presented. The calculations done by Ohya *et al.* still overestimate peak position as well as

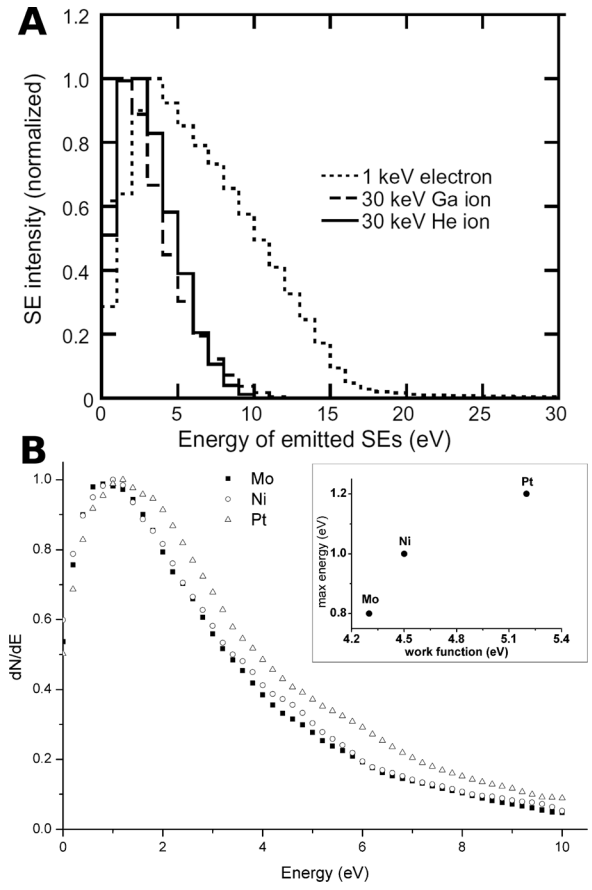

FIG. 3. SE yield in HIM. (a) Comparison of calculated SE yields for electrons, Ga ions, and He ions. Reproduced with permission from Ohya *et al.*, Nucl. Instrum. Meth. B **267**, 584 (2009). Copyright 2009, Elsevier B.V. (b) Experimentally obtained SE yield for three different metals. The dependence of the peak position on work function is shown as an inset. Reproduced with permission from Proc. SPIE **8036**, 80360O-1 (2011). Copyright 2011, SPIE.

peak width.[29] These differences between actual measurement results of SE yield in a HIM, and calculations are attributed to SE generation mechanisms not considered in the calculations. Indications exist that bulk plasmon excitations can play an important role[29,40] for SE generation in HIM. An actual measurement of SE yield as a function of SE energy and the work function dependence of the distribution maximum is presented in Fig. 3(b). A consequence of the particular energy distribution of SE in HIM and the small SE generation volume is an enhanced surface sensitivity. This has been shown in a recent comparative study of HIM and SEM imaging performance on carbon coated gold nanorods.[41] Only at very low acceleration voltages is SEM able to visualize the thin carbon layer covering the gold particles. However, low voltage SEM suffers from carbon deposition in the imaged area making detailed studies challenging. An example of the high sensitivity of HIM with respect to the material work function is the visualization of different half unit cell surface termination in Ti_3SiC_2.[42] Depending on the position of the cleavage plane, the surface is either terminated by Si (half unit cell) or Ti (full unit cell). The difference in the chemistry of the top surface layer of atoms results in different SE yields for the two terminations. As a result, they can be discriminated in HIM.

A software package called *IONiSE* developed by Rack and coworkers is available, which allows the calculation of the expected SE yield for a large number of materials.[30] Although good agreement has been achieved between simulation and experiment, only a limited number of analytical applications based on SE yield are known.[29]

Sample topography in HIM is made visible in a similar way as in SEM. The dependence of the SE yield on the specimen tilt with respect to the incoming beam can be described the following secant law:

$$\delta_{SE}(\theta) = \delta_{SE}(0)\sec\theta. \tag{4}$$

However, experimental studies showed that the actually measured SE yield at the detector deviates from the expected secant behavior.[31] The deviations lead to a more linear response curve, which in turn should reduce the strong edge effect known from SEM. Nevertheless, a very strong edge effect has been observed in thin layers.[43,44]

In summary, the achievable high resolution and surface sensitivity in HIM is based on the fact that the SEs originate from a cylinder at the beam penetration point with a diameter of approximately 1 nm—given by the beam diameter—and a length of less than 3 nm—determined by λ_d. This small probe volume helps to achieve a very high image resolution in HIM. It should be noted that obtaining such high resolution images has become substantially easier since the introduction of UHV HIM.[45] At small fields of views, usually high fluences are reached as a consequence of the large pixel density. In an UHV HIM, implantation and sputtering can still negatively affect the sample during imaging. Carbon deposition on the other hand can be excluded.[46] The removal of hydrocarbons from the sample chamber vacuum prevents the formation of carbon deposits in the imaged area. As a consequence, some exceptional imaging results could be achieved [see Fig. 6(b) later in the text].

2. Backscattered helium

What backscattered electrons are to the SEM, backscattered helium (BSHe) atoms and ions are to HIM. This rather bold statement is true in several ways, as will be highlighted in the next paragraphs.

Two different ways to utilize BSHe are available in current HIM. First, and most commonly used, is a microchannel plate (MCP) detector to acquire qualitative element distribution maps. Second, a silicon drift detector can be used to obtain spectroscopic information from microscopic areas. The latter allows quantitative element identification based on the same principles as Rutherford backscattering spectroscopy (RBS).

While SE images usually are rich in morphological contrast, BSHe images obtained with the MCP are poor in topography and rich in elemental contrast. In contrast to the SE images, the information in these images originates from the bulk of the sample. To measure them, the MCP is inserted below the pole piece in the primary beam path. While a center hole allows the primary beam to reach the sample, this geometry maximizes the solid angle, and thus the collection efficiency of the detector. The obtained contrast can be understood by examining the Rutherford scattering cross section

$$d\sigma = \left(\frac{q^2 Z_1 Z_2}{4E_0}\right)^2 \frac{d\Omega}{\sin^4\frac{\theta}{2}}, \tag{5}$$

where q is the elementary charge, and Z_1 and Z_2 denote the atomic number of impinging and target particle, respectively. Assuming that the target atom is at rest, E_0 is the energy of the impinging particle, $d\Omega$ is an arbitrary element of solid angle, and θ is the scattering angle. For fixed Z_1—helium for this review—and a given energy, a dependence on Z_2^2 leads to a strong contrast between different elements. A more detailed analysis of the scattering cross section shows that a dependence that is related to the structure of the periodic table of elements also exists. This is a result of the change in screening along the rows of the periodic table. In Fig. 4, experimentally obtained BSHe yields for various elements are presented. The dependence of the yield on the structure of the periodic table is clearly present.

At this point, it is important to realize that a high sensitivity is needed from the detector that is used. Under standard imaging conditions in HIM, typically 500 or less ions are used per pixel. Assuming a high backscatter yield of 20% and taking into account the detector solid angle, no more than 50 ions will reach the detector. A large fraction of these backscattered He particles are also neutral[47] due a charge transfer process, which occurs once they enter the sample. However, this would represent an ideal case for a heavy element bulk target. In practice, these numbers can be substantially smaller and not a single ion should be lost in the detector.[41]

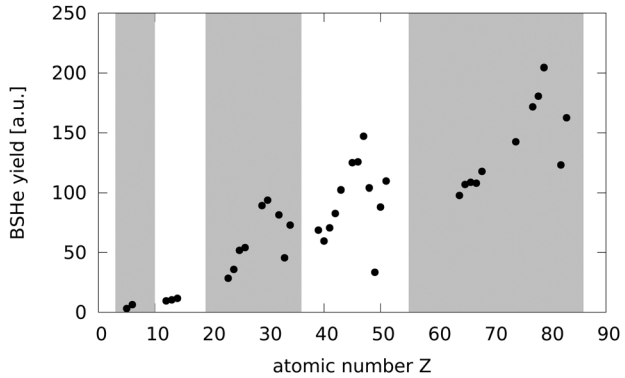

FIG. 4. Experimentally obtained backscattered Helium yield plotted against atomic number *Z*. The row structure of the periodic table can clearly be seen on top of a general increase in BSHe yield for heavy elements. Data courtesy of Carl Zeiss AG.

One should realize that contrary to the electrons discussed in the previous section, BSHe represents a bulk signal. Depending on the atomic number a sampling depth, between a few tens of nanometers and a few hundred nanometers can be achieved. As can be seen from Eq. (5), the backscatter efficiency can be increased by lowering the acceleration voltage. As a side effect, this will also reduce the range of the helium and thus the sampling depth.

In addition to the qualitative element distribution, also quantitative information on the elemental composition can be obtained. For a binary collision—when momentum and energy are conserved—the kinetic energy of the backscattered helium

$$E_1 = E_0\left(\frac{M_1}{M_1+M_2}\right)^2\left(\cos\theta \pm \sqrt{\left(\frac{M_1}{M_2}\right)^2 - \sin^2\theta}\right)^2 \tag{6}$$

depends on the ratio of the masses of the impinging (M_1) and target (M_2) particle. Measuring the energy loss at a fixed angle allows the mass of the collision partner, as well as its position relative to the sample surface, to be determined. At high keV or low MeV energies, this is known as RBS. This method is known to deliver high sensitivity and excellent depth-resolution. The nature of the involved square function makes the method very sensitive to differences between light elements. A silicon drift detector with a resolution of approximately 4 kV can be used for this purpose. However, due to the relatively low primary energy of only 35 keV, the measured peaks are not as well defined as in classical RBS. Nevertheless, the nature of HIM allows such spectra from areas of only several μm^2 to be obtained.[43] The technique has been successfully applied to measure ZrO_2 layer thicknesses on Si substrates with monolayer sensitivity[48] and for thickness measurements of cobalt/nickel nanorings.[43]

The achievable resolution is not only limited by the detector. As a result of the already low primary energy, the backscattered particles have a high probability to undergo multiple scattering events. This occurs for the impinging, as well the backscattered helium particle. Consequently, a statistical broadening of the exit energies of the BSHe exists. It has been shown by simulations that even for an ideal combination, such as a 75 nm thick heavy hafnium oxide film on silicon, an intrinsic uncertainty of 14% exists for the depth resolution of Hf. Given the current detector resolution, this value is further increased to 60%.[49] Compositional characterization will have even larger errors due to a severe peak overlap.[43] Figure 5 presents an experimentally obtained spectrum from hafnium oxide. The SIMNRA[48,50] calculated fits to obtain elemental composition, and layer thickness have been added for different real and ideal detector resolutions. An increase of detector resolution to 1 kV would substantially improve the quality of the obtained spectra and consequently of the fit accuracy. These curves should be taken to be an indication of what could be possible and not an exact representation of the achievable resolution. One also needs to keep in mind that the majority of the backscattered particles are neutral,[47,51] complicating any postscattering treatment.

The yield of both signals—secondary electrons as well as back scattered helium—also depends on the crystalline orientation of the sample with respect to the beam. This allows for two additional contrast mechanisms in HIM. The well known channeling contrast[31,39] can be exploited to obtain the crystal orientation of samples with a large lateral resolution.[46] This technique makes use of calculations of the blocked area fraction, which yields results similar to stereographic projections of channeling minima or Laue back reflection patterns.

One of the surprising results is that despite the very small wavelength of He ions, scanning transmission ion microscopy (STIM) is possible. Both dark field and bright field images could be recorded in which thickness fringes and line defects could be identified.[52]

3. Photons

Generally speaking, ionoluminescence (IL) is a phenomenon of light emission due to the optical transitions of an electronic system, which has been excited by ion irradiation. Three main stages can be distinguished in the luminescence process:[53,54]

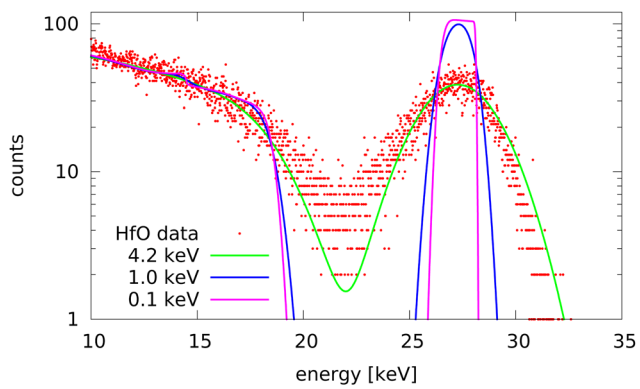

FIG. 5. (Color online) Experimentally obtained RBS data from a 4.2 nm hafnium oxide thin film on Si. The best fit to the data with the current used silicon drift detector and estimated profile shapes with detectors of 1 keV, and 100 eV resolution are presented.

(1) energy absorption and excitation of the electronic system;
(2) system relaxation and energy transfer to the emission centers;
(3) transition of the system into the ground state by photon emission.

During sample bombardment with He^+ ions, light can be obtained from the excited backscattered neutral He,[55,56] excited sputtered atoms and molecular complexes,[57–59] or from the sample material itself.[58,60] For the case where emission originates from excited species which have left the sample, the spectrum consists of discrete Doppler-broadened lines. These lines correspond to the optical transitions within atomic (or molecular) orbitals. This light is usually observed at a distance up to a few millimeters from the target surface.[58] In the case of organic samples, ionoluminescence reveals the electronic structure of the organic compounds.[61]

For the investigation of material properties, we are mainly interested in the luminescence from the sample itself. The physics of the emission processes is usually described by considering the sample's electronic band structure, or by using configuration coordinate diagrams.[53] According to its origin, there are two general types of luminescence: *extrinsic* and *intrinsic*.[62] In the case of extrinsic luminescence, the light generation is related to the presence of impurity atoms or ions (so-called *activators*) in the sample material. Depending on their electronic structure, activators can be divided in the following groups:

(1) transition metal ions with d^n electronic configuration (e.g., Ti^{3+}, Cr^{3+}, Mn^{2+});
(2) ions with s^2-configuration (e.g., Tl^+, Pb^{2+}, Sb^{3+});
(3) rare-earth elements ($REE^{2+/3+}$);
(4) actinides (e.g., UO_2^{2+}, Cm^{3+}).

Sometimes the presence of a certain impurity (*sensitizer*) is needed for the luminescence of an activator (for example, Ce^{3+} for activation of Tb^{3+} ions[63]). As opposed to sensitizers, *quenchers* suppress light emission from an activator. For example, Fe^{2+} ions act as quenchers for emission from Mn^{2+} in apatite.[64] At high activator concentrations, self-quenching may occur due to resonant absorption processes.

Intrinsic luminescence, on the other hand, is emission from the sample material itself. Two cases can be distinguished. First, optical transitions from delocalized states or, in other words, the recombination of free electrons from the conduction band with holes in the valence band. This can include direct and indirect transitions. The radiative recombination of free excitons also falls in this category. Second, optical transitions from localized states can also be attributed to intrinsic luminescence. This includes the following processes: recombination of excitons trapped at defect sites (so-called self-trapped excitons[65]), emission from excited defects—known as color centers (e.g., nitrogen-vacancy centers in diamond[66]), and transitions of charge carriers from delocalized into localized states. The shape and width of the emission peaks and bands strongly depends on electron–phonon interactions and thermal effects. A strong electron–phonon interaction leads to a Stokes shift and peak broadening. As a result, it is desirable to perform ionoluminescence measurements at cryogenic temperatures, which has not been done to date in HIM.

Since ionoluminescence is in many aspects similar to the cathodoluminescence (CL) phenomenon often observed in SEM, databases of CL studies can be employed for the interpretation of IL spectra. Ionoluminescence studies are significantly complicated by the fact that an ion beam not only induces light emission, but also directly influences the optical properties of the target due to defect creation. Ion irradiation can lead to target coloration (e.g., in alkali halides[67]) and enhanced emission, but also quench the luminescence (e.g., semiconductor materials[68]). However, the use of HIM to observe IL phenomena allows these processes to be followed *in-situ* with a high lateral resolution.

II. MICROSCOPY

In this section, we will try to give an overview of applications of helium ion microscopy that make use of the special imaging capabilities of the HIM. Although the high resolution is the most prominent fact that allows for very accurate critical dimension measurements,[69] many successful applications of HIM make use of other distinct characteristics of HIM. This overview is by no means complete but will attempt to highlight interesting and eventually surprising imaging applications.

A. Insulating and biological samples

The use of electrons for charge neutralization enables HIM to obtain high resolution images of insulating, and in particular uncoated, biological samples. In Fig. 6(a), a high resolution HIM image of a butterfly wing is presented.[70] The black ground scales of *Papilio ulysses* and other butterflies are imaged without any prior coating, which allows the smallest features to be identified. The large depth of field in HIM also makes it ideal for creating anaglyphs using different angles for imaging. High precision measurements of otherwise not accessible feature heights are possible this way.[70] However, only very few groups have demonstrated the applicability of HIM for imaging of cells.[32,71,72] This is astonishing since very high resolution should be possible. Figure 6 demonstrates the achievable resolution on such biological, soft, and insulating samples. The imaged protein crystal (flat bovine liver catalase) exhibits a simple rectangular unit cell with a lattice spacing of 8.8 nm × 6.7 nm. These values are in excellent agreement with the expected values from literature.[73]

B. Subsurface imaging

The use of BSHe for imaging allows among other things subsurface processes such as the formation of buried contacts to be visualized. This overcomes an existing limitation in how we currently try to follow subsurface diffusion processes. Helium ion microscopy offers a unique, destruction free method to reveal the in-plane shape of a diffusion front. In Fig. 7, results of a HIM study on the subsurface formation

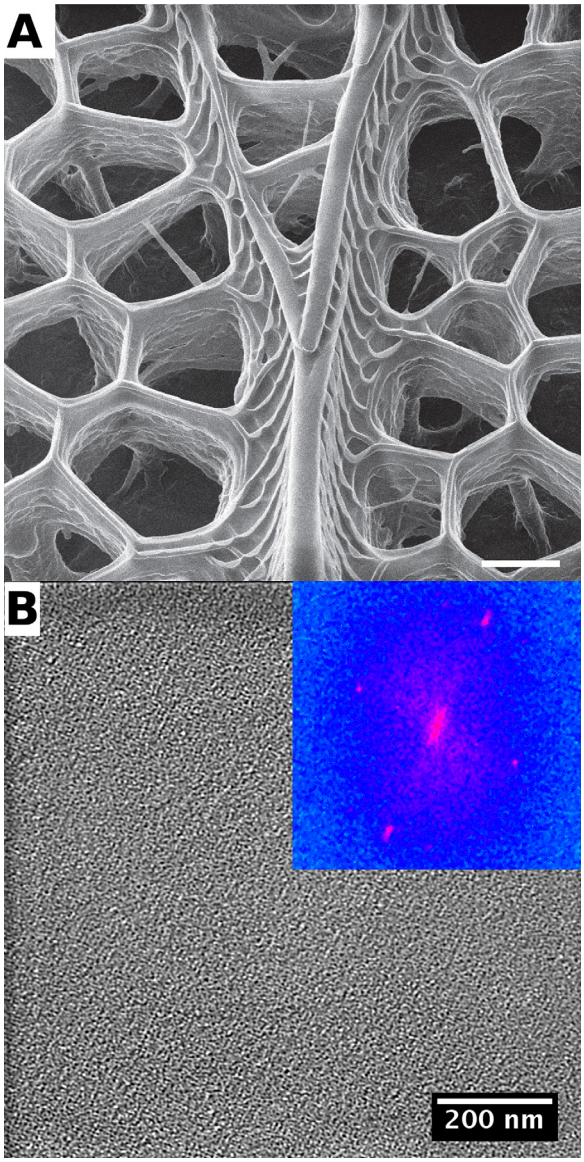

FIG. 6. (Color online) HIM imaging of biological samples. (a) High resolution image of uncoated *Papilio ulysses* black ground scales. The scale bar is 400 nm. Reproduced with permission from Boden *et al.*, Scanning **34**, 107 (2012). Copyright 2012, Wiley Periodical, Inc. (b) High resolution HIM image of flat bovine liver catalyze crystal. The inset FFT highlights the resolved lattice spacings. Image obtained on a UHV-HIM, courtesy of A. Lysse, Carl Zeiss Microscopy.

of Pd interconnects are presented.[74] While a large degree of surface detail is present in the SE image presented in Fig. 7(a), no direct indication of the buried Pd_2Si interconnect is visible. However, from the simultaneously recorded BSHe image shown in Fig. 7(b), the morphology of the Pd diffusion front can be seen. The benefit of this method over cross section approaches is evident. Besides the obvious ease with which the shape of curved interfaces can be resolved, sample preparation is also substantially easier. Knowledge of the nonstraight nature of the diffusion front is important to understand the reason for large variations in device performance. The shape of the subsurface diffusion front is not accessible using cross section techniques. Because the penetration depth of the ions can be varied by using different

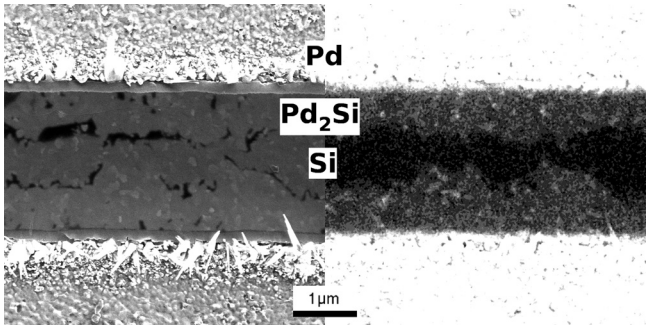

FIG. 7. Subsurface imaging in HIM. (a) Surface sensitive SE image obtained from SiO_2 covered Pd_2Si interconnects. (b) Simultaneously recorded BSHe image showing the Pd deposits (bright, top and bottom) and the buried Pd_2Si layer. The shape of the two Pd diffusion fronts is clearly discernible in between the two Pd contacts.

primary energies, it is also possible to get an estimate of the thickness of the cover layer.[74]

C. Ionoluminescence

There are several reviews[58,75,76] introducing various applications of IL for material characterization that also reveal possible complications of the technique. Here, we will focus on IL imaging with light ions and results obtained with HIM.

The possibility to do IL imaging using a HIM was demonstrated by Boden *et al.*[68] The authors tested a wide range of samples such as quantum dots (QDs), semiconductors, rare-earth doped nanocrystals, and Ce^{3+} doped garnet. Both bulk samples and nanocrystals doped with REE were found to exhibit IL. This is a result of the optical transitions of the *f* electrons in the dopant. However, the IL signal was found to decay with prolonged beam exposure. This decay has been attributed to defect accumulation, which hinders electron transport to the actual emitting rare-earth atoms.

Several direct bandgap semiconductor materials were investigated in Ref. 68, but no IL was detected. However, recently we managed to obtain clear ionoluminescence information from such a material. Figure 8 shows the IL image obtained from a thin GaN film on sapphire using a fluence of only $3 \times 10^{12}\,\mathrm{cm}^{-2}$. The dark lines in the IL image (Fig. 8) are dislocations that are initially present in the film. These act as centers for nonradiative recombination[77] and appear dark. The black dot with the gray halo in the center of the image is the result of the long term irradiation of a single pixel prior to recording the image. Due to the high dose applied there, all IL is quenched rapidly. This is the result of the creation of various types of defects that provide nonradiative paths for the electron de-excitation.[78]

In contrast to bulk semiconductors, the authors of Ref. 68 could record IL images of agglomerates of semiconductor quantum dots. It is suggested that crystal defects in QDs are generated at a lower rate due to the small size of the particles (≈5 nm). Hard nuclear collisions occur deeper in the bulk, while in the first tens of nanometers electronic stopping is predominant. The observed emission corresponds to the

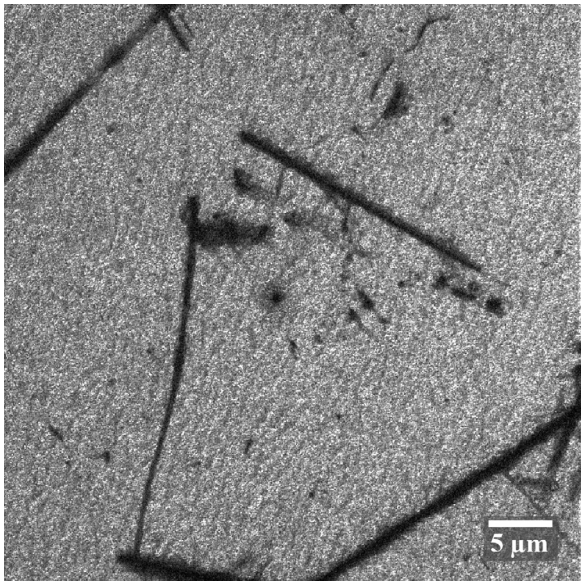

FIG. 8. IL image of a GaN surface. He^+ beam energy is 35 keV. FOV: 45 μm.

expected bandgap transition. Nevertheless, the signal is quenched with increasing ion fluence. While QD aggregates were detected with relative ease, attempts to record IL images with higher magnification showing single QDs were not successful.

Alkali halides are known to exhibit intrinsic IL as a result of defect production due to the ion beam radiation.[79–81] Figure 9 demonstrates simultaneously acquired images of residues from NaCl solution on a metal substrate. The bright areas in the SE image [Fig. 9(a)] are the aluminum substrate. The darker areas that exhibit a rough appearance are NaCl and residue from the drop-cast solution used. The IL image [Fig. 9(b)] clearly shows the presence of NaCl as bright ramified structures.

Ogawa *et al.*[82] have reported IL measurements on SiO_2 using HIM. Interestingly, they observe an increase of the IL intensity with increasing fluence. The authors identify several differences between CL and IL spectra from the same sample, but the nature of the IL signal remains unclear.

The use of IL for analysis of biological samples is possible, but not very often used. The advantage of IL imaging over conventional fluorescence imaging is an absence of diffraction limits that restrict the spatial resolution. In that respect, application of IL in HIM for bioimaging looks promising. Few groups have used proton beams with energies in the MeV range to investigate biological samples such as cells[83] and skin tissue.[61] In another study, several promising dyes have been identified and can now be used to stain cells specifically for IL investigations.[84] However, only limited work is done using IL for imaging of biological samples. Using a classical ion source, a resolution of 150 nm has been demonstrated for ionoluminescence images in STIM mode.[85]

D. Imaging of thin and soft layers

Graphene, the prototypical thin layer that currently receives a lot of attention, has successfully been imaged by several groups.[31,44,86–88] This was done for both suspended and free standing graphene. In Fig. 10, a SiO_2 supported graphene flake has been imaged using mild imaging conditions. The flakes can be imaged easily with substantial contrast, despite their ultrathin nature. The sequence of images presented in Fig. 10 shows the formation and collapse of helium filled bubbles. Graphene has been shown to be impermeable for many gases including helium;[89] hence, the backscattered helium remains trapped below the graphene sheet. These bubbles fill with He until either the rim of the flake or a hole in the layer is reached. This will allow the He to escape and the bubble then collapses. This process can be observed for the central bubble between doses of $2.0 \times 10^{14}\,cm^{-2}$ (initial filling) and $2.3 \times 10^{14}\,cm^{-2}$ (collapse and start of refilling). The filling of the bubbles and subsequent deformation of the graphene sheet results in the stretching of wrinkles and folds that are present in the sheet. Assuming that the bubble has the shape of a spherical cap with a height of 100 nm and a diameter of 4 μm we can calculate the pressure under the graphene sheet. Using the ideal gas law and a backscatter yield

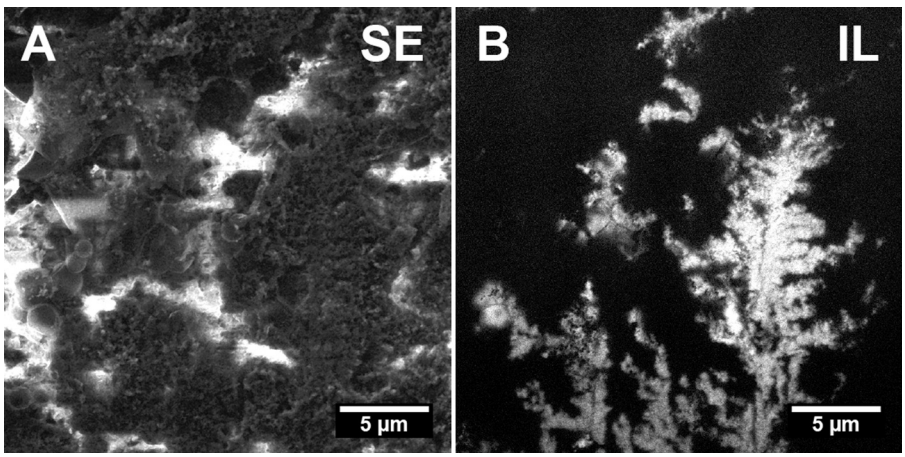

FIG. 9. Simultaneously recorded SE and IL images of NaCl residues from water solution on a metal. IL images reveal a distribution of NaCl. He^+ beam energy is 35 keV. FOV: 25 μm.

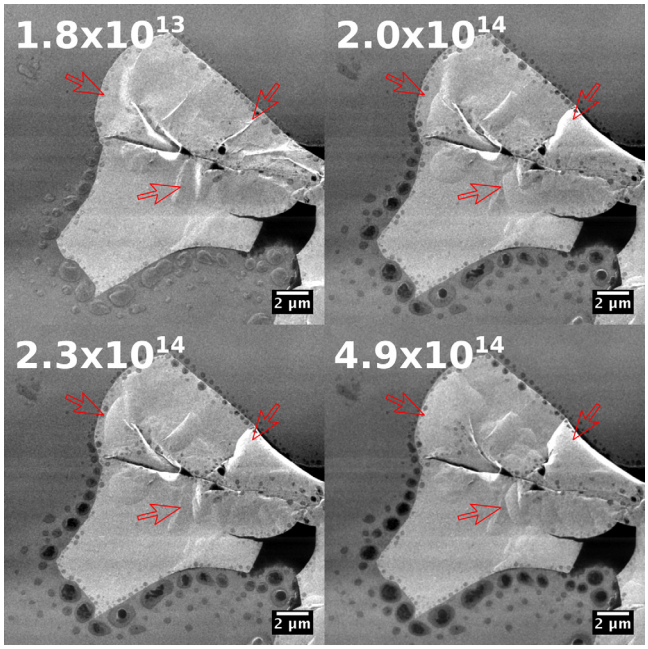

FIG. 10. (Color online) Graphene flake on SiO_2. Using a dose of $1.8 \times 10^{13}\,cm^{-2}$ per image the formation of a He bubble can be observed. As can be seen for the bubble marked in the lower part of the images, holes and edges allow the He to escape and the bubble collapses. At a fluence of $2.0 \times 10^{14}\,cm^{-2}$, the bubble is filled, and it collapses two frames later after increasing the dose to $2.3 \times 10^{14}\,cm^{-2}$. With further increase of the dose the cycle starts again. FOV is $20\,\mu m$. Ion doses in cm^{-2} are indicated in the figures.

of 0.006, as obtained from SRIM,[90] we arrive at a pressure on the order of 10 mbar. This value agrees reasonably well with the observed pressure range for gas bubbles under graphene on SiO_2 obtained elsewhere.[89]

First principles calculations indicate that it should be possible to reveal the graphene lattice using HIM due to minute changes in the electron emission across the lattice.[91] However, the realization of such an image might be difficult due to the destructive nature of the helium beam. It is not clear if sufficient signal can be collected before the defects will alter the local atomic configuration.[44] Defects created in graphene due to the ion–graphene interaction have been investigated theoretically.[92–94] Recent experimental investigations indicate that already at very low doses severe damage is done to the graphene sheet and many defects are created.[44] Safe imaging doses for suspended graphene seem to be as low as 10^{13}–$10^{14}\,cm^{-2}$.[44] For supported graphene, as shown above, the critical dose is certainly lower due to the more destructive nature of recoils from the support material.

An exceptional imaging result has been achieved for carbon nanomembranes (CNMs).[95] Such free standing membranes, which are formed by cross linking self-assembled monolayers (SAMs) and then removing the substrate, are difficult to image using conventional SEM. However, in HIM, these CNMs are not only visible, but morphological details such as folds and nanometer sized holes created by slow highly charged ions are also visible.[96]

Given the nature of ultrathin films and the sampling volume of the available secondary imaging particles in HIM, the SEs are the obvious choice for imaging such samples. An example of the successful application of HIM to soft layers is the visualization of the phase separation in a mixed poly(3-hexylthiophene)/[6,6]-phenyl-C_{61}-butric acid methyl ester.[97] Such blends are typically used in organic photovoltaic solar cells and represent an important materials class. Although both molecules are essentially carbon, the different number of π and σ bonds in the two polymers results in minute changes of the SE yield.[98] An other example is the clear identification of SAM deposited onto SiO_2.[99,100] Here, differences in work function allow the identification of SAM molecules and give rise to the observed contrast.

A delicate method of visualizing noncontinuous ultrathin layers and their different properties utilizes BSHe. For a substrate oriented in a channeling condition, a very low BSHe signal is recorded due to the extended range of He along the low index channeling direction.[46] However, at places where a thin surface layer with different atomic positions is present, scattering will occur and an increased BSHe signal can be observed. Although the relative mass of the elements in the adlayers and the underlying bulk are important, this effect works for any combination of bulk and adlayer elements.[101] In particular, it works for light elements on a heavy substrate.[99,100]

E. Voltage contrast

Similar to SEM, local electromagnetic fields in the sample will influence the yield, angular distribution, and energy of the generated SE. This can be utilized to image dopant distribution[102] and electronic potential distribution. A similar application utilizes static capacitive[103] contrast to reveal conducting features buried below an insulating cover.[32]

III. MATERIALS MODIFICATION

The availability of different gases for GFIS—such as neon[104,105]—and the combination with a classic liquid metal gallium FIB[106,107] makes the technique interesting for various types of materials modifications. The fine beam produced by the GFIS has the potential to engineer structures with a length scale that is well below what is currently possible with LMIS based FIB techniques. Contrary to e-beam writing, which can achieve similar critical lengths, the removal of material is also possible.

A. Resist patterning

Writing structures into resists is usually done using gas injection systems in FIB or, if higher resolutions are needed, by using e-beam lithography. In particular, the latter suffers from the so-called proximity effect.[108] The deposition parameters necessary to achieve a constant feature size will depend on the distance to the next feature in the proximity of the beam. This effect is a consequence of the relatively large lateral range of the electrons in the resist material. Structures produced by low mass ion beams are less sensitive to this effect.[13] The near complete absence of this effect is related

to the fact that in the surface near region there is practically no scattering when using ion beams (see also Fig. 2). Furthermore, very little backscattering occurs in the usually relatively light resist materials. In addition, the very low energy SE (<10 eV)[29,30,38,39] in HIM are localized close to the beam path, whereas the SEs in e-beam lithography have a higher energy (>100 eV) and therefore travel relatively long distances in the resist material.[109] As a consequence, resist modification by ions happens only in a very small volume along the beam path. An extensive overview comparing electrons and ions for their useful application in lithography is given by Melngailis.[110]

With the availability of He GFIS, new standards have been set in terms of achievable line width.[111–114] This has at least partially been made possible by the above discussed, near complete, absence of the proximity effect when using a highly focused He beam. However, to date, resists initially developed for e-beam lithography such as hydrogen sylsesquioxane and polymethyl methacrylate resist are used. New resist materials optimized for the large amount of energy deposited by the ion beam could potentially lead to even better results.

B. Beam induced deposition

Several precursor materials have been explored including $MeCpPtMe_3$, TEOS, and XeF_2.[112,115–118] Recently, also a tungsten based metal precursor has successfully been used.[119] With this extremely flexible method, a wide range of features can be directly sculpted including 3D structures. Figure 11 shows examples of structures created using ion beam induced deposition in the group of Alkemade.[114] However, a detailed understanding of the deposition process is needed to unleash the full potential of the method for resist patterning. A model has been proposed that identifies primary ions and secondary electrons as being responsible for the vertical growth of the structures. Scattered ions and recoil atoms on the other hand are responsible for the lateral growth of the structures.[120] Simulation software (*EnvisION*) based on this model is available and can be used to predict the metal deposition process in HIM.[115] The program is based on available concepts and code of an electron-beam-induced simulation[121] and the *IONiSE*[30] Monte Carlo program. Experimental confirmation of results showed the applicability of the simulation method.[115]

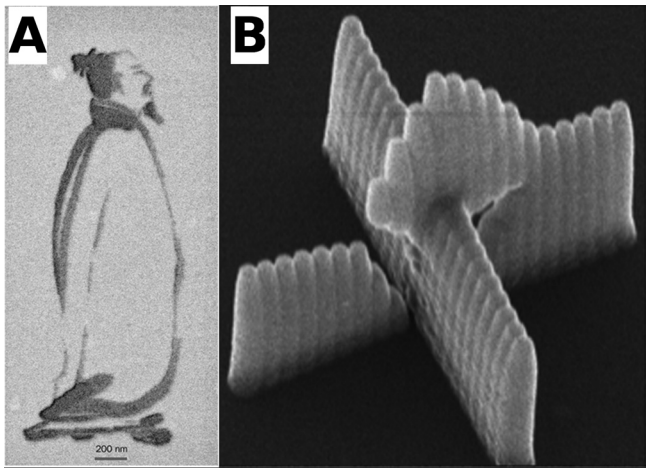

FIG. 11. Examples of structures created using He beam induced metal deposition. (a) 100.000× demagnified copy of a 13th century painting of the Chinese poet Li Bai. (b) Stacked cross formed by exploiting shadowing of the precursor gas (FOV: 1 μm). Adapted with permission from Alkemade *et al.*, Scanning 34, 90 (2012). Copyright 2012, Wiley Periodicals, Inc.

C. Direct write lithography

Different from what has been discussed in the previous section, here we will discuss structuring results that do rely on the sputtering of sample atoms. Sputtering is a well known phenomenon that has been extensively studied.[122–124] However, with only a few exceptions, these works usually focus on ions of lower energies of only a few hundred eV to a few keV for the relevant gases helium and neon. For higher energy ranges, the bombardment species is either not a noble gas or generally a heavier element. The energy range of interest for HIM is not so well investigated. Surprisingly, many as yet unexplained phenomena, such as very high and fluence dependent sputter yields are observed.[125] Due to the subnanometer size and the collimated nature of the HIM ion beam, it is possible to mill features with very small critical dimensions not possible with current FIB technology. We start by discussing results obtained on the most simple milled structure—a pore. Such pores are successfully used for biomolecule detection. The achievable diameter can be as small as 4 nm, which is 60% smaller compared to other one step milling techniques.[126] Most importantly, the quality of these pores for biomolecule detection is comparable to state-of-the-art pores fabricated using TEM[127] or FIB.[128] However, these techniques create smallest pores by closing the existing bigger pores in a controlled way. The method relies on the fluidization of the material under irradiation and subsequent deformation which is driven by the surface tension and diffusion of ad-atoms created by an ion beam.[127,128] Although it has not been demonstrated to date, this should also be possible by careful implantation of He into the area surrounding the pore. In addition to the effects observed elsewhere,[127,128] an additional volume increase and subsequent reduction of pore size can occur due to the formation of nanosized He bubbles.[129,130] Substantial redistribution of unsputtered material has already been observed when milling bigger pores.[131] As a result, comparable diameters should be achievable.

Recently, a GFIS using neon[132] became available. Its combination with a classical liquid metal gallium FIB column allows for efficient milling of structures at several length scales.[106] Figure 12 shows a structure milled into gold using all three beams. While initial cut outs are made using the LMIS gallium source [Fig. 12(a)], finer details are cut using the GFIS and neon [Fig. 12(b)]. Smallest details with a length scale of the order of 10 nm are patterned using helium and the GFIS [Fig. 12(c)]. The same gas source combination is also used for imaging of the structures.

Another exciting application of helium ion beams for direct write lithography is the successful preparation of devices based on graphene.[133] The possibility to precisely cut graphene with nanometer precision has been demonstrated

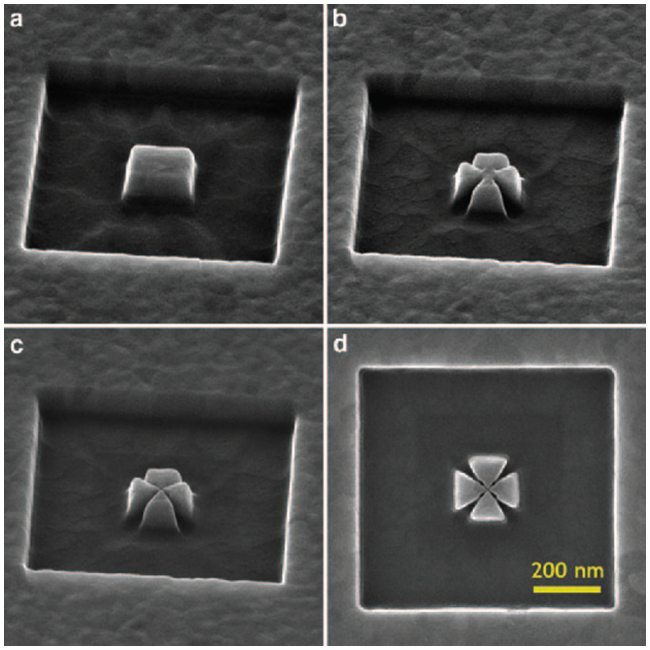

FIG. 12. (Color online) Milling a gold on glass substrate over multiple length scales. (a) The initial structure is milled using a gallium beam. (b) Intermediate features are milled using a GFIS neon beam. (c) Final milling of details is performed with a He ion beam. (d) Achievable feature sizes are as small as 13 nm. Reproduced with permission from Notte, Microsc. Today **20**, 16 (2012). Copyright 2012, Microscopy Society of America.

earlier by Lemme *et al.*[86] Unfortunately, the unique properties of graphene are very sensitive to damage introduced by the impinging ions.[134] Consequently, only very small fluences of the order of 10^{13} cm^{-2} can be used to image graphene without damaging it to the extent that the unique properties are lost.[44] Unfortunately, this excludes high resolution imaging of supported as well as free standing graphene.

D. Helium implantation and defect engineering

Helium implantation is unavoidable in HIM. It is therefore important to understand the associated defect structures, their evolution, and response to external influences. It has to be made clear that the phenomena discussed in this section appear at doses higher than those normally used in HIM imaging. However, special applications (BSHe or IL imaging) may require relatively high doses. Obviously, He implantation plays an important role when the HIM is used for materials modification, as discussed in the previous section. A dramatic example is shown in Ref. 135 in the context of the fabrication of domain wall magnetoresistance devices. Although successful fabrication of domain wall magnetoresistance devices was demonstrated at lower doses, at higher doses, the implanted He leads to a swelling and surface deformation that in turn results in the destruction of the patterned devices.

Initial studies that allow the comparison of experimental damage volumes with SRIM were made by Livengood *et al.*[136] One of the results in this publication is summarized in an overview over the different damage regimes that are to be expected for a wide range of He doses (see Fig. 13). Interestingly, this diagram is valid for both semiconductor

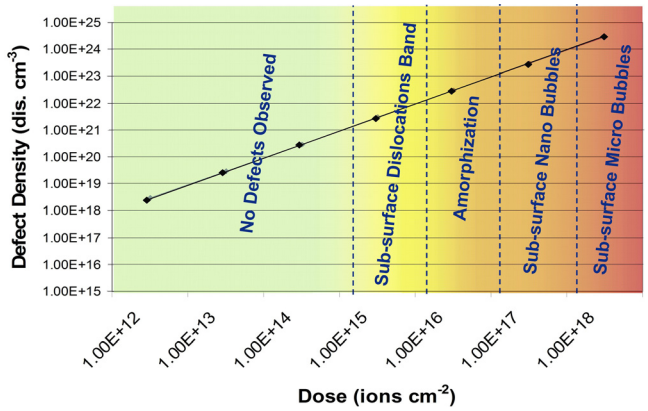

FIG. 13. (Color online) Defect density vs He ion dose for silicon and copper. The regimes in which specific damage mechanisms dominate are marked. Reproduced with permission from Livengood *et al.*, J. Vac. Sci. Technol. B **27**, 3244 (2009). Copyright 2009, American Vacuum Society.

materials (silicon) and metals (copper). The validity of these damage regimes has been demonstrated by several groups. A nice visualization of the bubbles that form at depths comparable to the range of the ions in the material is shown by Ref. 130. The pressure inside these bubbles and blisters is high. For the rather soft and ductile metal gold, pressures of up to several GPa can be reached in the initial He nanobubbles.[129] These bubbles form at open volume defects that are either present in the material or are created by the beam.[137,138] The growth of these initial, nanosized, He bubbles is independent of the primary energy and leads to observable materials modification at fluences in the low 10^{17} cm^{-2} range.[129,136] However, with increasing He dose, these bubbles start to coalesce, provided they are formed deep enough in the sample to not immediately reach the sample surface. What follows is a rapid expansion of a blister on the surface. The pressure inside such a blister of a few hundred MPa (Refs. 129 and 135) is substantially lower than in the initial nanosized bubbles. The effective formation and rapid growth of He induced blisters is at least partly due to the fact that highly compressed He gas is an ideal stopping medium for He. This results in an amplification of the damage in the vicinity of the bubble and the observed accelerated growth.

IV. SUMMARY

In the past half decade, helium ion microscopy has proven to be an interesting alternative to its direct and well established competitors: scanning electron microscopy and gallium focused ion beam. However, the authors strongly believe, and hope to have demonstrated above, that HIM is more than a replacement for SEM and FIB. It excels over SEM and FIB in particular for

(1) high resolution imaging of uncoated biological samples
(2) imaging of insulating samples
(3) a high surface sensitivity
(4) imaging of ultrathin layers
(5) materials modification with unprecedented resolution
(6) direct write lithography
(7) resist patterning.

At the same time, new applications and techniques are constantly being developed and refined. In particular, analytical additions are needed and are currently being developed. While ionoluminescence has its special applications, additions such as secondary ion mass spectroscopy[139] still need to prove their applicability in real materials science problems. However, although spectroscopy is currently still in its infancy, the extension of the technique to other gases such as neon, and potentially even heavier ones, guarantees an exciting future of the technique in particular for nanofabrication applications.

ACKNOWLEDGMENTS

This research was supported by the Dutch Technology Foundation STW, which is the applied science division of NWO, and the Technology Programme of the Ministry of Economic Affairs.

[1]V. N. Tondare, J. Vac. Sci. Technol. A **23**, 1498 (2005).
[2]L. Bischoff, Ultramicroscopy **103**, 59 (2005).
[3]J. L. Hanssen, S. B. Hill, J. H. Orloff, and J. J. McClelland, Nano Lett. **8**, 2844 (2008).
[4]Q. Ji, X. Jiang, T.-J. King, K.-N. Leung, K. Standiford, and S. B. Wilde, J. Vac. Sci. Technol. B **20**, 2717 (2002).
[5]J. I. Goldstein *et al.*, *Scanning Electron Microscopy and X-ray Microanalysis*, 3rd ed. (Springer, Berlin, 2003).
[6]I. Utke, P. Hoffmann, and J. Melngailis, J. Vac. Sci. Technol. B **26**, 1197 (2008).
[7]M. Knoll and E. Ruska, Zeitschrift für Phys. **78**, 318 (1932).
[8]J. H. Orloff and L. W. Swanson, J. Appl. Phys. **50**, 6026 (1979).
[9]K. Horiuchi, T. Itakura, and H. Ishikawa, J. Vac. Sci. Technol. B **6**, 937 (1988).
[10]M. Sato, Jpn. J. Appl. Phys. **31**, L291 (1992).
[11]W. H. Escovitz, T. R. Fox, and R. Levi-Setti, Proc. Natl. Acad. Sci. U.S.A. **72**, 1826 (1975).
[12]J. H. Orloff and L. W. Swanson, J. Vac. Sci. Technol. **12**, 1209 (1975).
[13]T. Itakura, K. Horiuchi, and S. Yamamoto, Microelectron. Eng. **3**, 153 (1985).
[14]K. Horiuchi, T. Itakura, and H. Ishikawa, J. Vac. Sci. Technol. B **6**, 241 (1988).
[15]E. W. Müller, Zeitschrift für Phys. **131**, 136 (1951).
[16]A. J. Melmed, Appl. Surf. Sci. **94–95**, 17 (1996).
[17]B. W. Ward, J. A. Notte, and N. P. Economou, J. Vac. Sci. Technol. B **24**, 2871 (2006).
[18]S. Kalbitzer, Appl. Phys. A **79**, 1901 (2004).
[19]J. L. Pitters, R. Urban, C. Vesa, and R. A. Wolkow, Ultramicroscopy **131**, 56 (2013).
[20]R. Urban, R. A. Wolkow, and J. L. Pitters, Ultramicroscopy **122**, 60 (2012).
[21]R. Urban, J. L. Pitters, and R. A. Wolkow, Appl. Phys. Lett. **100**, 263105 (2012).
[22]J. L. Pitters, R. Urban, and R. A. Wolkow, J. Chem. Phys. **136**, 154704 (2012).
[23]F. H. M. Rahman, J. A. Notte, R. H. Livengood, and S. Tan, Ultramicroscopy **126**, 10 (2013).
[24]J. H. Orloff, M. Utlaut, and L. W. Swanson, *High Resolution Focused Ion Beams: FIB and Its Applications* (Springer, Boston, MA, 2003).
[25]H. H. Rose, *Geometrical Charged-Particle Optics*, Springer Series in Optical Sciences, Vol. 142 (Springer, Berlin, 2009).
[26]N. Ernst, G. Bozdech, H. Schmidt, W. Schmidt, and G. L. Larkins, Appl. Surf. Sci. **67**, 111 (1993).
[27]R. Hill, J. A. Notte, and B. W. Ward, Phys. Procedia **1**, 135 (2008).
[28]J. A. Notte *et al.*, AIP Conf. Proc. **931**, 489 (2007).
[29]Y. V. Petrov and O. F. Vyvenko, Proc. SPIE **8036**, 80360O-1 (2011).
[30]R. Ramachandra, B. J. Griffin, and D. C. Joy, Ultramicroscopy **109**, 748 (2009).
[31]D. C. Bell, Microsc. Microanal. **15**, 147 (2009).
[32]L. Scipioni, C. A. Sanford, J. A. Notte, B. Thompson, and S. McVey, J. Vac. Sci. Technol. B **27**, 3250 (2009).
[33]H. A. Bethe, Phys. Rev. **59**, 913 (1941).
[34]K. Ohya, K. Inai, A. Nisawa, and A. Itoh, Nucl. Instrum. Meth. B **266**, 541 (2008).
[35]M. Rösler, "Theory of ion–induced kinetic electron emission from solids," in *Ionization of Solids by Heavy Particles*, NATO ASI Series, edited by R. A. Baragiora (Plenum, New York, 1985), pp. 27–58.
[36]Y. Lin and D. C. Joy, Surf. Interface Anal. **37**, 895 (2005).
[37]J. Ferrón, E. Alonso, R. Baragiola, and A. Oliva-Florio, Phys. Rev. B **24**, 4412 (1981).
[38]K. Ohya, T. Yamanaka, K. Inai, and T. Ishitani, Nucl. Instrum. Meth. B **267**, 584 (2009).
[39]Y. V. Petrov, O. F. Vyvenko, and A. S. Bondarenko, J. Surf. Investig. **4**, 792 (2010).
[40]P. Riccardi, P. Barone, A. Bonanno, A. Oliva, and R. Baragiola, Phys. Rev. Lett. **84**, 378 (2000).
[41]G. Hlawacek, I. Ahmad, M. A. Smithers, and E. S. Kooij, Ultramicroscopy **135**, 89 (2013).
[42]K. Buchholt, P. Eklund, J. Jensen, J. Lu, A. L. Spetz, and L. Hultman, Scr. Mater. **64**, 1141 (2011).
[43]G. Behan, D. Zhou, M. Boese, R. M. Wang, and H. Z. Zhang, J. Nanosci. Nanotechnol. **12**, 1094 (2012).
[44]D. Fox, Y. B. Zhou, A. O'Neill, S. Kumar, J. J. Wang, J. N. Coleman, G. S. Duesberg, J. F. Donegan, and H. Z. Zhang, Nanotechnology **24**, 335702 (2013).
[45]R. van Gastel *et al.*, Microsc. Microanal. **17**, 928 (2011).
[46]V. Veligura, G. Hlawacek, R. van Gastel, H. J. W. Zandvliet, and B. Poelsema, Beilstein J. Nanotechnol. **3**, 501 (2012).
[47]G. Behan, J. F. Feng, H. Z. Zhang, P. N. Nirmalraj, and J. J. Boland, J. Vac. Sci. Technol. A **28**, 1377 (2010).
[48]S. Sijbrandij, J. A. Notte, L. Scipioni, C. Huynh, and C. A. Sanford, J. Vac. Sci. Technol. B **28**, 73 (2010).
[49]R. van Gastel, G. Hlawacek, S. Dutta, and B. Poelsema, "Backscattered helium spectroscopy in the helium ion microscope: Principles, resolution and applications," in *IOP Conference Series: Material Science and Engineering* (European Microbeam Analysis Society, Porto, 2013).
[50]M. Mayer, AIP Conf. Proc. **541**, 541 (1999).
[51]D.-E. Arafah, J. Meyer, H. Sharabati, and A. Mahmoud, Phys. Rev. A **39**, 3836 (1989).
[52]J. A. Notte, R. Hill, S. M. McVey, R. Ramachandra, B. J. Griffin, and D. C. Joy, Microsc. Microanal. **16**, 599 (2010).
[53]A. S. Marfunin, "Luminescence," in *Spectroscopy, Luminescence and Radiation Centers in Minerals* (Springer, Berlin, Heidelberg, 1979), Chap. 5, pp. 141–222.
[54]J. Götze and U. Kempe, "Physical principles of cathodoluminescence (CL) and its applications in geosciences," in *Cathodoluminescence and Its Application in the Planetary Sciences*, edited by A. Gucsik (Springer, Berlin, 2009), Chap. 1, pp. 1–22.
[55]C. Kerkdijk and E. Thomas, Physica **63**, 577 (1973).
[56]W. Baird, M. Zivitz, and E. Thomas, Phys. Rev. A **12**, 876 (1975).
[57]W. F. van der Weg and P. K. Rol, Nucl. Instrum. Meth. **38**, 274 (1965).
[58]C. W. White, Nucl. Instrum. Meth. **149**, 497 (1978).
[59]N. H. Tolk, I. S. T. Tsong, and C. W. White, Anal. Chem. **49**, 16A (1977).
[60]D. Ghose and R. Hippler, "Ionoluminescence," in *Luminescence of Solids*, edited by D. R. Vij (Springer, Berlin, 1998), pp. 189–220.
[61]J. Pallon, C. Yang, R. Utui, M. Elfman, K. Malmqvist, P. Kristiansson, and K. Sjöland, Nucl. Instrum. Meth. B **130**, 199 (1997).
[62]U. Scherz, "Grundlagen der Festkörperphysik," in *Lehrbuch der Experimentalphysik*, 2nd ed., edited by R. Kassing (Gruyter, Berlin, 1992), pp. 1–107.
[63]M. V. Hoffman, J. Electrochem. Soc. **118**, 1508 (1971).
[64]G. M. Filippelli and M. L. Delaney, SEPM J. Sediment. Res. **63**, 167 (1993).
[65]R. Williams and K. Song, J. Phys. Chem. Solids **51**, 679 (1990).
[66]M. W. Doherty, N. B. Manson, P. Delaney, F. Jelezko, J. Wrachtrup, and L. C. Hollenberg, Phys. Rep. **528**, 1 (2013).
[67]K. Schwartz, "Excitons and radiation damage in alkali halides," in *Atomic Physics Methods in Modern Research*, Lecture Notes in Physics, Vol. 1, edited by K. P. Jungmann, J. Kowalski, I. Reinhard, and F. Träger (Springer, Berlin, 1997), pp. 351–366.
[68]S. A. Boden, T. M. W. Franklin, L. Scipioni, D. M. Bagnall, and H. N. Rutt, Microsc. Microanal. **18**, 1253 (2012).
[69]M. T. Postek, A. Vladár, C. Archie, and B. Ming, Meas. Sci. Technol. **22**, 024004 (2011).

[70]S. A. Boden, A. Asadollahbaik, H. N. Rutt, and D. M. Bagnall, Scanning **34**, 107 (2012).
[71]W. Jiang, V. Shutthanandan, B. Arey, and A. Lea, "Helium ion microscopy of microstructures and biological samples," in *Microscopic Microanalysis* (Portland, 2010), available at http://www.microscopy.org/MandM/2010/jiang.pdf.
[72]M. S. Joens *et al.*, Sci. Rep. **3**, 3514 (2013).
[73]R. Luftig, J. Ultrastruct. Res. **20**, 91 (1967).
[74]R. van Gastel, G. Hlawacek, H. J. W. Zandvliet, and B. Poelsema, Microelectron. Reliab. **52**, 2104 (2012).
[75]P. Townsend, M. Khanlary, and D. Hole, Surf. Coat. Technol. **201**, 8160 (2007).
[76]P. Townsend, Nucl. Instrum. Meth. B **286**, 35 (2012).
[77]T. Sugahara *et al.*, Jpn. J. Appl. Phys. **37**, L398 (1998).
[78]S. O. Kucheyev, M. Toth, M. R. Phillips, J. S. Williams, C. Jagadish, and G. Li, Appl. Phys. Lett. **78**, 34 (2001).
[79]V. Veligura, G. Hlawacek, R. van Gastel, H. J. W. Zandvliet, and B. Poelsema, "High resolution ionoluminescence study of defect creation and interaction" (unpublished).
[80]A. Bazhin, E. Rausch, and E. Thomas, Phys. Rev. B **14**, 2583 (1976).
[81]M. Aguilar, P. J. Chandler, and P. D. Townsends, Radiat. Eff. **40**, 1 (1979).
[82]S. Ogawa, T. Iijima, S. Awata, R. Sugie, N. Kawasaki, and Y. Otsuka, Microsc. Microanal. **18**, 814 (2012).
[83]F. Watt, A. Bettiol, J. V. Kan, M. Ynsa, R. Minqin, R. Rajendran, C. Huifang, S. Fwu-Shen, and A. Jenner, Nucl. Instrum. Meth. B **267**, 2113 (2009).
[84]P. Rossi *et al.*, Nucl. Instrum. Meth. B **181**, 437 (2001).
[85]R. Norarat, V. Marjomäki, X. Chen, M. Zhaohong, R. Minqin, C.-B. Chen, A. Bettiol, H. Whitlow, and F. Watt, Nucl. Instrum. Meth. B **306**, 113 (2013).
[86]M. C. Lemme, D. C. Bell, J. R. Williams, L. A. Stern, B. W. H. Baugher, P. Jarillo-Herrero, and C. M. Marcus, ACS Nano **3**, 2674 (2009).
[87]D. Pickard *et al.*, "Graphene nanoribbons fabricated by helium ion microscope," in *Bulletin of the American Physical Society*, Vol. 55 (American Physical Society, Portland, Oregon, 2010).
[88]S. Nakaharai, T. Iijima, S. Ogawa, S. Suzuki, S.-l. Li, K. Tsukagoshi, S. Sato, and N. Yokoyama, ACS Nano **7**, 5694 (2013).
[89]J. S. Bunch, S. S. Verbridge, J. S. Alden, A. M. van der Zande, J. M. Parpia, H. G. Craighead, and P. L. McEuen, Nano Lett. **8**, 2458 (2008).
[90]J. F. Ziegler, J. P. Biersack, and M. D. Ziegler, SRIM, *the Stopping and Range of Ions in Matter* (SRIM Co., Chester, 2008).
[91]H. Zhang, Y. Miyamoto, and A. Rubio, Phys. Rev. Lett. **109**, 265505 (2012).
[92]O. Lehtinen, J. Kotakoski, A. V. Krasheninnikov, and J. Keinonen, Nanotechnology **22**, 175306 (2011).
[93]E. H. Ålgren, J. Kotakoski, O. Lehtinen, and A. V. Krasheninnikov, Appl. Phys. Lett. **100**, 233108 (2012).
[94]O. Lehtinen, J. Kotakoski, A. V. Krasheninnikov, A. Tolvanen, K. Nordlund, and J. Keinonen, Phys. Rev. B **81**, 153401 (2010).
[95]A. Turchanin and A. Gölzhäuser, Prog. Surf. Sci. **87**, 108 (2012).
[96]R. Ritter *et al.*, Appl. Phys. Lett. **102**, 063112 (2013).
[97]A. J. Pearson, S. A. Boden, D. M. Bagnall, D. G. Lidzey, and C. Rodenburg, Nano Lett. **11**, 4275 (2011).
[98]Y. Kishimoto, T. Ohshima, M. Hashimoto, and T. Hayashi, J. Appl. Polym. Sci. **39**, 2055 (1990).
[99]G. Hlawacek, V. Veligura, S. Lorbek, T. F. Mocking, A. George, R. van Gastel, H. J. W. Zandvliet, and B. Poelsema, Beilstein J. Nanotechnol. **3**, 507 (2012).
[100]A. George, M. Knez, G. Hlawacek, D. Hagedoorn, H. H. J. Verputten, R. van Gastel, and J. E. ten Elshof, Langmuir **28**, 3045 (2012).
[101]T. F. Mocking, G. Hlawacek, and H. J. W. Zandvliet, Surf. Sci. **606**, 924 (2012).
[102]M. A. E. Jepson, B. J. Inkson, C. Rodenburg, and D. C. Bell, Europhys. Lett. **85**, 46001 (2009).
[103]K. Ura and S. Aoyagi, J. Electron Microsc. (Tokyo) **49**, 157 (2000).
[104]F. H. M. Rahman, S. McVey, L. Farkas, J. A. Notte, S. Tan, and R. H. Livengood, Scanning **34**, 129 (2012).
[105]R. H. Livengood, S. Tan, R. Hallstein, J. A. Notte, S. McVey, and F. H. Rahman, Nucl. Instrum. Meth. A **645**, 136 (2011).
[106]J. A. Notte, Microsc. Today **20**, 16 (2012).
[107]H. M. Wu *et al.*, Nanotechnology **24**, 175302 (2013).
[108]T. H. P. Chang, J. Vac. Sci. Technol. **12**, 1271 (1975).
[109]M. P. Seah and W. A. Dench, Surf. Interface Anal. **1**, 2 (1979).
[110]J. Melngailis, Nucl. Instrum. Meth. B **80–81**, 1271 (1993).
[111]D. Winston *et al.*, J. Vac. Sci. Technol. B **27**, 2702 (2009).
[112]D. J. Maas, E. van Veldhoven, P. Chen, V. Sidorkin, H. W. M. Salemink, E. van der Drift, and P. F. A. Alkemade, "Nanofabrication with a helium ion microscope," in *Metrology, Inspection, and Process Control for Microlithography XXIV*, edited by C. J. Raymond (SPIE, San Jose, 2010), Vol. 7638, p. 763814.
[113]E. van der Drift and D. J. Maas, *Nanofabrication: Techniques and Principles*, edited by M. Stepanova and S. Dew (Springer, Vienna, 2012), pp. 93116.
[114]P. F. A. Alkemade, E. M. Koster, E. van Veldhoven, and D. J. Maas, Scanning **34**, 90 (2012).
[115]P. Chen, E. van Veldhoven, C. A. Sanford, H. W. M. Salemink, D. J. Maas, D. A. Smith, P. D. Rack, and P. F. A. Alkemade, Nanotechnology **21**, 455302 (2010).
[116]L. Scipioni, C. A. Sanford, E. van Veldhoven, and D. J. Maas, Micros. Today **19**, 22 (2011).
[117]P. F. A. Alkemade and E. van Veldhoven, "Deposition, milling, and etching with a focused helium ion beam," *in Nanofabrication: Techniques and Principles*, edited by M. Stepanova and S. Dew (Springer, Vienna, 2012), pp. 275–300.
[118]C. A. Sanford, L. Stern, L. Barriss, L. Farkas, M. DiManna, R. Mello, D. J. Maas, and P. F. A. Alkemade, J. Vac. Sci. Technol. B **27**, 2660 (2009).
[119]K. Kohama, T. Iijima, M. Hayashida, and S. Ogawa, J. Vac. Sci. Technol. B **31**, 031802 (2013).
[120]P. F. A. Alkemade, P. Chen, E. van Veldhoven, and D. J. Maas, J. Vac. Sci. Technol. B **28**, C6F22 (2010).
[121]D. A. Smith, J. D. Fowlkes, and P. D. Rack, Nanotechnology **19**, 415704 (2008).
[122]P. Sigmund, Nucl. Instrum. Meth. B **27**, 1 (1987).
[123]M. Thompson, Phys. Rep. **69**, 335 (1981).
[124]*Sputtering by Particle Bombardment, Topics in Applied Physics*, Vol. 110, edited by R. Behrisch and W. Eckstein (Springer, Berlin, Heidelberg, 2007).
[125]C. Fowley, Z. Diao, C. C. Faulkner, J. Kally, K. Ackland, G. Behan, H. Z. Zhang, a. M. Deac, and J. M. D. Coey, J. Phys. D. Appl. Phys. **46**, 195501 (2013).
[126]J. Yang, D. C. Ferranti, L. A. Stern, C. A. Sanford, J. Huang, Z. Ren, L.-C. Qin, and A. R. Hall, Nanotechnology **22**, 285310 (2011).
[127]A. J. Storm, J. H. Chen, X. S. Ling, H. W. Zandbergen, and C. Dekker, J. Appl. Phys. **98**, 014307 (2005).
[128]J. Li, D. Stein, C. McMullan, D. Branton, M. J. Aziz, and J. A. Golovchenko, Nature **412**, 166 (2001).
[129]V. Veligura, G. Hlawacek, R. P. Berkelaar, R. van Gastel, H. J. W. Zandvliet, and B. Poelsema, Beilstein J. Nanotechnol. **4**, 453 (2013).
[130]D. Fox, Y. Chen, C. C. Faulkner, and H. Z. Zhang, Beilstein J. Nanotechnol. **3**, 579 (2012).
[131]M. M. Marshall, J. Yang, and A. R. Hall, Scanning **34**, 101 (2012).
[132]S. Tan, R. H. Livengood, D. Shima, J. A. Notte, and S. McVey, J. Vac. Sci. Technol. B **28**, C6F15 (2010).
[133]S. A. Boden, Z. Moktadir, D. M. Bagnall, H. Mizuta, and H. N. Rutt, Microelectron. Eng. **88**, 2452 (2011).
[134]M. Lucchese, F. Stavale, E. H. M. Ferreira, C. Vilani, M. Moutinho, R. B. Capaz, C. A. Achete, and A. Jorio, Carbon N. Y. **48**, 1592 (2010).
[135]Y. Wang, S. A. Boden, D. M. Bagnall, H. N. Rutt, and C. H. de Groot, Nanotechnology **23**, 395302 (2012).
[136]R. H. Livengood, S. Tan, Y. Greenzweig, J. A. Notte, and S. McVey, J. Vac. Sci. Technol. B **27**, 3244 (2009).
[137]J. Laakmann, P. Jung, and W. Uelhoff, Acta Metall. **35**, 2063 (1987).
[138]H. Rajainmäki, S. Linderoth, H. Hansen, R. Nieminen, and M. Bentzon, Phys. Rev. B **38**, 1087 (1988).
[139]T. Wirtz, N. Vanhove, L. Pillatsch, D. Dowsett, S. Sijbrandij, and J. A. Notte, Appl. Phys. Lett. **101**, 041601 (2012).
[140]H. Demers, N. Poirier-Demers, A. R. Couture, D. Joly, M. Guilmain, N. de Jonge, and D. Drouin, Scanning **33**, 135 (2011).
[141]R. Hill and F. H. M. Rahman, Nucl. Instrum. Meth. A **645**, 96 (2011).